Simulation of Free-Surface Flows Induced by Partially Immersed Moving Body: Validation

T. Jongen
Unilever Research, P.O. Box 114, 3133 AT Vlaardingen, The Netherlands

S. M. Chouikhi
Unilever Research, Sharnbrook, Bedford MK44 1LQ, United Kingdom

Predictive performance of a free-surface simulation technique is assessed using the volume-of-fluid (VoF) method, in the context of a challenging, yet simple and well-defined, unsteady-flow configuration mimicking the in-mouth kinematic processes occurring during the consumption of liquid foods. An experimental "mouth-analog" setup consisting of a cavity initially filled with a liquid and agitated by a ram moving periodically was modeled and simulated. Experimental and computational results are compared for a range of liquid viscosities (silicon oil and water) and over a range of processing conditions (low- and high-agitation frequency) that trigger important effects such as surface reconnection and breakup, wall coating, filament formation, and air inclusion. Even with the large mesh and time-step sizes used in the computations, the main relevant bulk kinematics of this complex transient free-surface flow can be represented with a Euler volume-tracking method such as the VoF method.

Introduction

The prediction of the flow of two immiscible fluids separated by a well-defined interface is of interest for many industrial applications. The efficient numerical simulation of these flows still constitutes a challenge, especially when the motion of the free surface is complex and subjected to large topological deformations. In the area of food processing for instance, free-surface flows are ubiquitous, from jar-filling and batch mixing applications to the flow of liquid food and saliva in the mouth during product consumption. It is actually the latter example that motivates the present study. The release of flavors in the mouth during consumption of liquid foods involves a number of physicochemical phenomena that have to be taken into account in any modeling and simulation effort. Among them are the simulation of free-surface flows induced by internal moving bodies (the tongue and the jaw); the transport of mass (the flavor) within the bulk food and saliva mixture, its transfer across the deformable liquid/gas interface (food and saliva/air), and its transport in the head space (the buccal and nasal cavities); the thermal transfer between the body and the food; the rheological changes of the food as a consequence of shear forces, and thermal and concentration changes; and the geometrical complexity of the simulation domain (buccal cavity shape, including tongue motion and deformation, teeth). The success of the overall simulation relies on the capability of adequately modeling and simulating all these phenomena separately. In this context, the primary aim of this work is to evaluate and assess a method for simulating the unsteady motion of a liquid with free surfaces. The present study focuses on a test case involving a simple geometry with a simple moving body, the "mouth-analog," and two immiscible and segregated fluid phases having a Newtonian rheology. This simple flow configuration is used to test the technique in a number of modes directly relevant to the parent in-mouth consumption problem. Experimental data on the same test configuration have been gathered in order to carefully assess the ability to capture the most relevant features of the transient flows gener-

---

Correspondence concerning this article should be addressed to T. Jongen.

ated, including surface merging and breakup, wall coating, and air inclusion. Future work based on these results will then help to answer questions related to the sensory perception of food ("mouthfeel") as far as its relation to the dynamics of stress distribution on the solid surfaces is concerned. Other issues, such as the influence of mixing on the transfer of flavors to the headspace, could also be further understood.

The remainder of the article is organized as follows. The following section gives more details about the numerical technique used to simulate free surface flows, while the third section presents the experimental setup used for the comparisons with the simulations, which are discussed in the fourth section. Finally, some conclusions are drawn in the last section.

Free-Surface Simulation Method

The volume of fluid (VoF) method (Hirt and Nichols, 1981) is a standard technique for simulating two-phase flows with discrete interfaces (Tezduyar et al., 1992). Used in the context of a mesh-based computational algorithm, it is in principle able to track large and complex deformations of the interface, and lends itself to a simple implementation. The interface between the two phases is represented by the discontinuity in an auxiliary scalar field (the volume of fluid, or the volume fraction), which is advected as a Lagrangian invariant. The sharpness of this discontinuity is especially difficult to maintain in time, and surface sharpening techniques have to be used (Lafaurie et al., 1994) to prevent excessive smearing out of the interface location as the computations evolve. The inclusion of interfacial effects, such as surface tension and contact angle, is done using the continuum surface force (CSF) method (Brackbill et al., 1992), which poses additional difficulties that have to be evaluated as well. Finally, the presence of the internal moving body is taken into account by using a deforming body-fitted mesh.

Governing equations

The governing equations for each phase $\alpha = 1, 2$ are conservation of mass and conservation of momentum. Since there are only two phases, the phase-volume fractions ϕ_α are related by $\phi_2 = 1 - \phi_1$, and only one conservation equation for the phase-volume fractions has to be solved, say for $\phi = \phi_1$. Moreover, the requirement that the two phases are immiscible, or segregated, means that ϕ can only take the values 0 or 1 at any point. In this case, there will be only one phase present at any point of the domain. Thus, one global transport equation for velocity field $u_i = u_i^\alpha$ is sufficient for both phases. In this case, the governing equations written here for incompressible fluids are,

$$\frac{\partial}{\partial t}\phi + u_j \frac{\partial}{\partial x_j}\phi = 0, \tag{1}$$

and

$$\frac{\partial}{\partial t}u_i + u_j \frac{\partial}{\partial x_j}u_i = -\frac{1}{\rho}\frac{\partial}{\partial x_i}p + \nu \frac{\partial^2}{\partial x_j^2}u_i + g_i + F_i, \tag{2}$$

where p is the pressure, $\rho = \phi\rho_1 + (1-\phi)\rho_2$ is the local density, $\nu = \phi\nu_1 + (1-\phi)\nu_2$ is the local kinematic viscosity, g_i is the gravitational acceleration vector component, and F_i represents the volumetric surface-tension force.

Inclusion of surface-tension effects

The continuum surface force (CSF) method (Brackbill et al., 1992) interprets the surface-tension force as a continuous volumetric effect across an interface. This effect is modeled as additional gradient forces that arise in the momentum equations at the interface between phases and where the interface touches a wall. The method is applicable to fluids in which the surface tension coefficient is constant and the surface tension force acts normal to the phase interface. More precisely, the surface tension force is defined in terms of the gradient of an auxiliary color function (Brackbill et al., 1992), which can be taken here as the phase-volume fraction ϕ,

$$F_i = w\sigma\kappa \frac{\partial}{\partial x_i}\phi, \tag{3}$$

where σ is the surface-tension coefficient, w is a density weighting factor that is used to ease the convergence of the numerical scheme in the case of large density differences (Burt et al., 1996), and κ is the surface curvature, given by

$$\kappa = -\frac{\partial}{\partial x_j}\left(\frac{n_j}{\sqrt{n_i n_i}}\right), \tag{4}$$

where n_i is the normal vector to the free surface, $n_i = (\partial/\partial x_i)\phi$.

Wall adhesion

Wall adhesion is the surface force acting on the fluid interface at the points of contact with the wall. In a static condition the surface force is balanced by a pressure gradient, observed as a surface curvature. A line drawn tangential to the curved surface touching the wall makes an angle with the wall known as the static equilibrium contact angle. In the case of a fluid interface moving along a wall, the contact angle may vary as some function of a local variable. In most cases, however, it is sufficient to model the moving interface with a constant dynamic equilibrium contact angle. In the present implementation of the wall adhesion boundary condition, the free-surface normal and the phase-volume fraction, ϕ, at the wall are repeatedly modified until the equilibrium contact angle condition is satisfied. Changing the surface normal at the wall modifies the curvature and introduces an additional force calculated from Eq. 3. This force tends to move the interface toward the desired contact angle and balances the pressure gradient at convergence. More details on the implementation can be found in Burt et al. (1996).

Discretization and numerical solution

The presence of a solid body moving within the computational mesh has been taken into account by using a body-fitted deforming grid. Since the computations are performed in a fixed reference frame, an arbitrary Lagrangian-Eulerian deforming mesh [ALE-DM; (Hirt et al., 1974; Donea et al., 1982)] formulation of the governing equations (Eqs. 1 and 2)

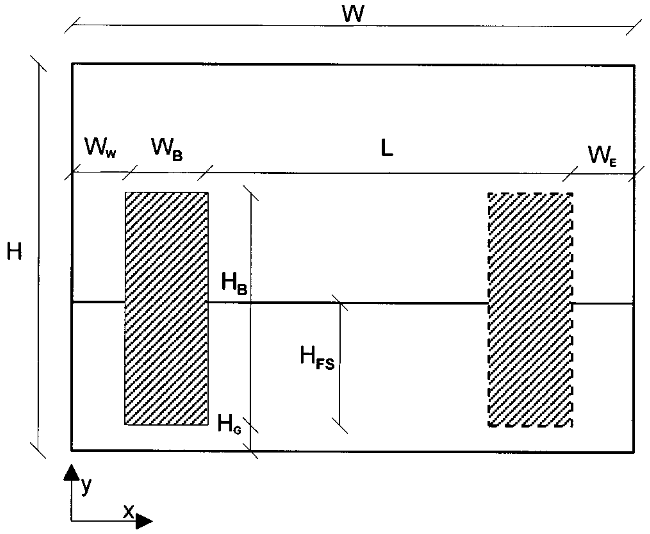

Figure 1. Geometry of the transient free-surface generation device.

has been used in order to account for the grid velocity in the advection terms and the volume changes of the grid cells. The mesh nodes deform during the motion of the body, and the presence of the latter has been accounted for by considering that the nodes covered by the body have a prescribed velocity (the body velocity), and no discrete form of the governing equations is solved for them.

Simulations have been carried out using the general-purpose finite-volume computational fluid dynamics package CFX-4.2 from AEA Technology, Ltd. (CFDS, 1995). This code uses a colocated cell-centered finite-volume approach, in combination with the Rhie–Chow algorithm (Rhie and Chow, 1983), in the context of the simple pressure correction scheme (Patankar, 1980). Special treatment of the surface-tension forces is included to avoid unphysical checkerboard oscillations of the free surface. A well-known drawback of Euler-based methods is that the standard convective treatment for the transport of the phase-volume fraction can produce an excessive numerical diffusion, leading to a spreading of the interfacial region. The origins of this diffusivity and a means of limiting it are discussed in Lafaurie et al. (1994) and Ubbink and Issa (1999). In the present work, sharp interfaces are maintained by reconstructing the free surface at each time step with a (mass-conserving) surface-sharpening algorithm, as described in CFDS (1995).

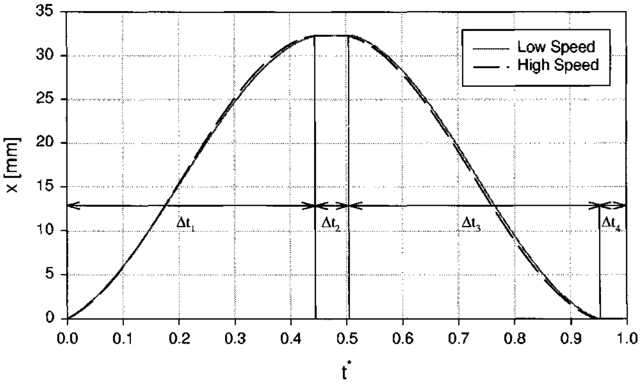

Figure 2. Successive positions of the ram over one cycle ($0 \leq t^* \leq 1$), for the two agitation regimes used in the experiments.

Note the dwell times where the ram is not moving during the two time intervals Δt_2 and Δt_4.

Experimental Setup

The transient-flow generation device, sketched in Figure 1, consists of a closed cavity partially filled with a liquid, and containing a solid ram moving periodically along the horizontal coordinate. The variation in time of the ram position can be described by the relation

$$x(t^*) = a_p + b_p \cos\left(c_p t^* + d_p\right), \tag{5}$$

where $t^* = t/T$ is a normalized time, with T the cycle time, and $p = 1, \ldots, 4$ identifies the time segment, Δt_p, for which the coefficients a_p, b_p, c_p, and d_p take different values. The decomposition of the ram motion (Eq. 5) into four segments allows the representation of dwell times where the ram is not moving, as observed experimentally when the ram reaches one of its two extreme positions, as shown in Figure 2. Two different speeds of the ram have been considered in the experiments, a low-speed case, for which $T = 4.47$ s, and a high-speed case, where $T = 0.903$ s. Table 1 summarizes the values of the time intervals and the coefficients for both cases, while the geometrical dimensions of the cavity, the ram, and the initial fill level are given in Table 2. Finally, Table 3 contains an overview of the material properties of the two different fluids used in the cavity. Fast video-imaging acquisition techniques are used to capture and extract the instantaneous free-surface topology, which is then used for quantitative comparison with the numerical simulations.

Table 1. Parameters Characterizing the Cyclic Motion of Ram at Different Stroke Speeds

T [s]	4.470				0.903			
p	1	2	3	4	1	2	3	4
Δt_p [s]	2.000	0.300	1.940	0.230	0.402	0.050	0.400	0.050
a_p [mm]	15.706	32.300	16.094	0.000	15.793	32.300	16.036	0.000
b_p [mm]	−16.730	0.000	16.560	0.000	−16.543	0.000	16.414	0.000
c_p [1/s]	1.331	0.000	1.390	0.000	6.897	0.000	6.977	0.000
d_p	0.739	0.000	−2.864	0.000	−5.961	0.000	−9.354	0.000

Table 2. Geometrical Parameters Characterizing Cavity and Initial Fill Height

W	W_B	W_W	W_E	H	H_B	H_G	L	H_{FS}	Width (z-Direction)
47	6	4	6	34	20	1	33	10	30

Note: All values are given in mm.

Simulation Results

The computations have been performed on a two-dimensional cross-section of the cavity (Figure 1), assuming the effects of the front and back walls (at fixed z-coordinates) to be limited. Also, the simulations did not take into account the cylindrical shaft used in the experimental configuration to move the ram. A body-fitted deforming mesh (shown in Figure 3) has been used, with a total of 110 control volumes in the x-direction, and 150 control volumes in the y-direction. Note that the ram covers the same nodes at all times, leading to a stretching (squeezing) in the x-direction of the nodes in the fluid domain that are on the trailing (leading) edge of the ram. The size of the time steps used for marching in time were dependent on the viscosity of the filling liquid, but were for both cases of the order of $T/100$.

For each of the four cases that have been investigated (two liquid viscosities and two stroke frequencies), a qualitative comparison based on instantaneous free-surface topologies will be presented together with a more quantitative assessment based on the time evolution of the free-surface height at fixed x positions. In both cases, the free-surface location is defined as the level $\phi = 1/2$. Note that due to space limitations, only the most representative snapshots of these essentially transient problems are shown over the ram's first cycle of motion.

It is instructive to estimate the values taken by several relevant dimensionless parameters for each of the cases considered. In addition to the Reynolds (Re) number, the Froude (Fr) and Capillary (Ω) numbers are obvious candidates, as both gravity and surface-tension effects are involved in the

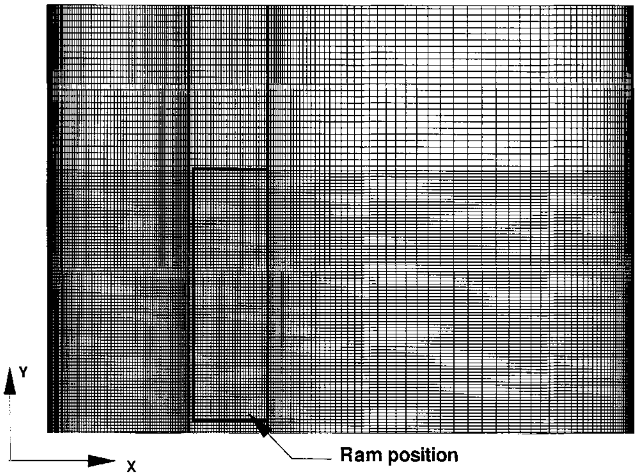

Figure 3. Computational mesh used for the simulations.

The grid has nodes coinciding with the moving ram, and deforms with its motion.

Table 3. Material Properties of Two Liquids in the Cavity

	Silicon Oil	Water
μ [Pa·s]	1.076	0.001
ρ [kg/m^3]	998	998
σ [N/m]	0.225	0.0725
α [deg]	10	25

Table 4. Values of Relevant Adimensional Numbers for the Cases Considered

	$\overline{U}$	Re	Fr	Ω
Oil at 16 rpm	1.47×10^{-2}	0.27	1.1×10^{-3}	0.07
Water at 16 rpm	1.47×10^{-2}	293	1.1×10^{-3}	2×10^{-4}
Oil at 52 rpm	7.31×10^{-2}	1.35	2.7×10^{-2}	0.34
Water at 62 rpm	7.31×10^{-2}	1,461	2.7×10^{-2}	1.1×10^{-3}

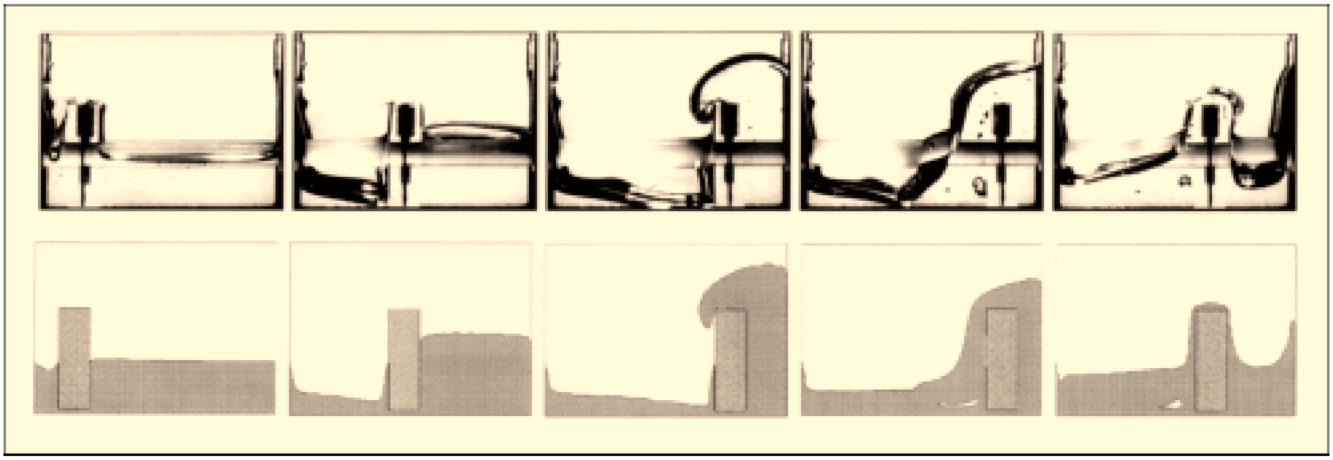

Figure 4. Free surface at different times for silicon oil at low speed.

From left to right: $t^* = 0.00$; $t^* = 0.17$; $t^* = 0.43$; $t^* = 0.50$; $t^* = 0.70$. Experiments are shown on the top row.

present flow. The definition of those numbers is

$$Re=\frac{\overline{U}H_B}{\nu},\qquad Fr=\frac{\overline{U}^2}{gH_B},\qquad \Omega=\frac{\mu\dot{\gamma}}{\sigma/R}, \tag{6}$$

where $\overline{U}=2L/T$ is the representative velocity scale, taken here as the average ram velocity over one sweep, and the length scale has been taken as the cam height, H_B. In the definition of the capillary number, Ω, the representative shear rate can be taken as $\dot{\gamma}=\overline{U}/H_B$, and the typical radius of curvature $R=H_B$ as well. Table 4 gives the numerical values of these dimensionless numbers for the four cases considered. From the values of the Reynolds number, one can conclude that the cases involving the oil will be laminar, with very little inertial effects. The main transient modes involved with the flow will be the ones corresponding to the cam motion. In the case of water, the relatively large values of the Reynolds number indicate that the flow should evolve in the time toward a turbulent state, with smaller flow structures present, and many additional (inertial) modes will coexist with the one corresponding to the cam motion. The small value of the Froude number in all the cases indicates that gravity plays a dominant role, and the segregation between the phases is expected to return rapidly to a horizontal direction. Finally, the low capillary numbers suggests that the breakup of filaments into drops will not be a dominant phenomenon.

Oil at 16 rpm

As can be seen in Figure 4, most of the features of the free-surface deformation are reproduced in the simulations, including the bulging over the ram and the coating on the side walls. Note also the presence of the shaft in the experi-

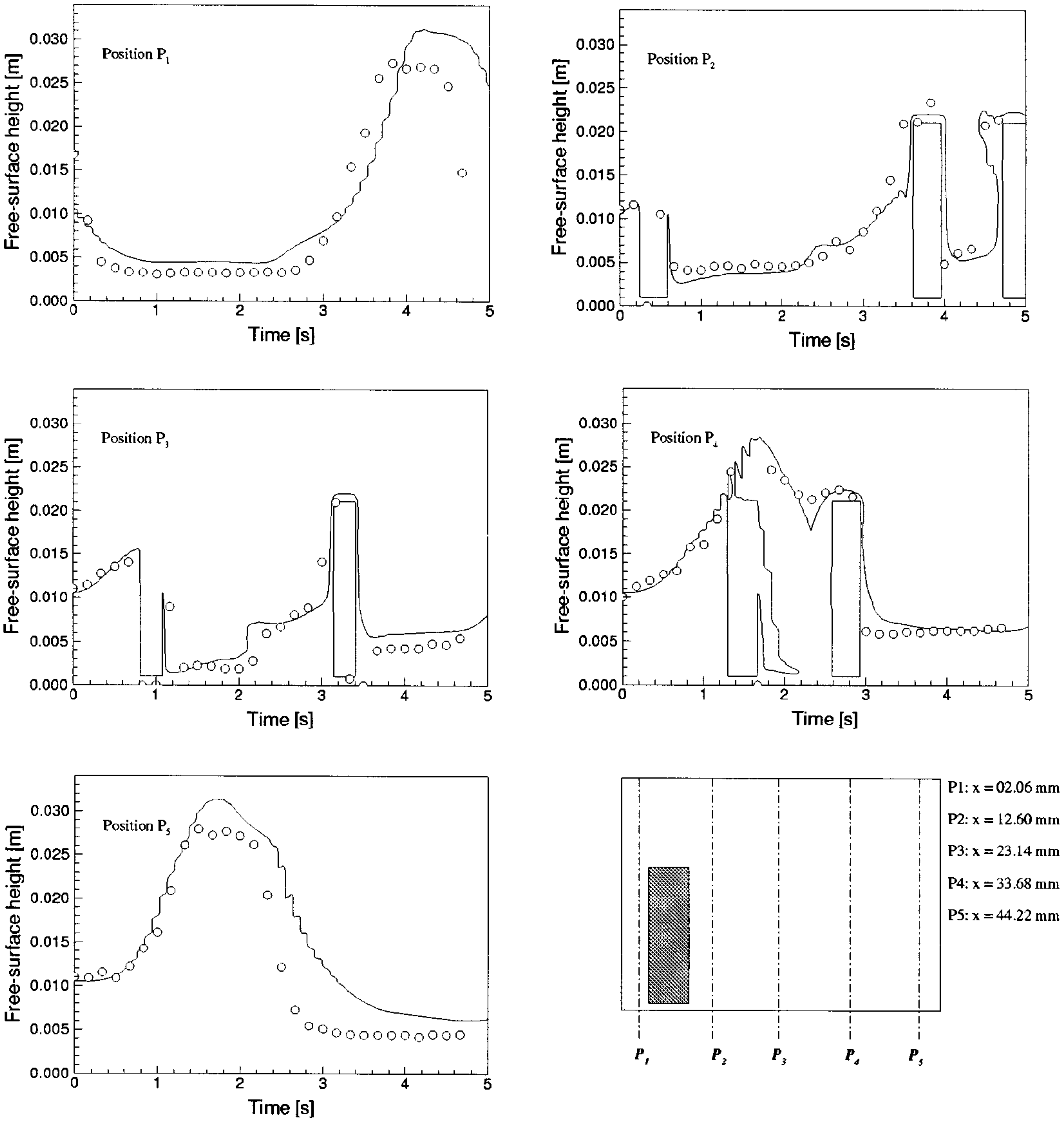

Figure 5. Free-surface height comparison: silicon oil at low speed.

○: experiments; ——: simulations.

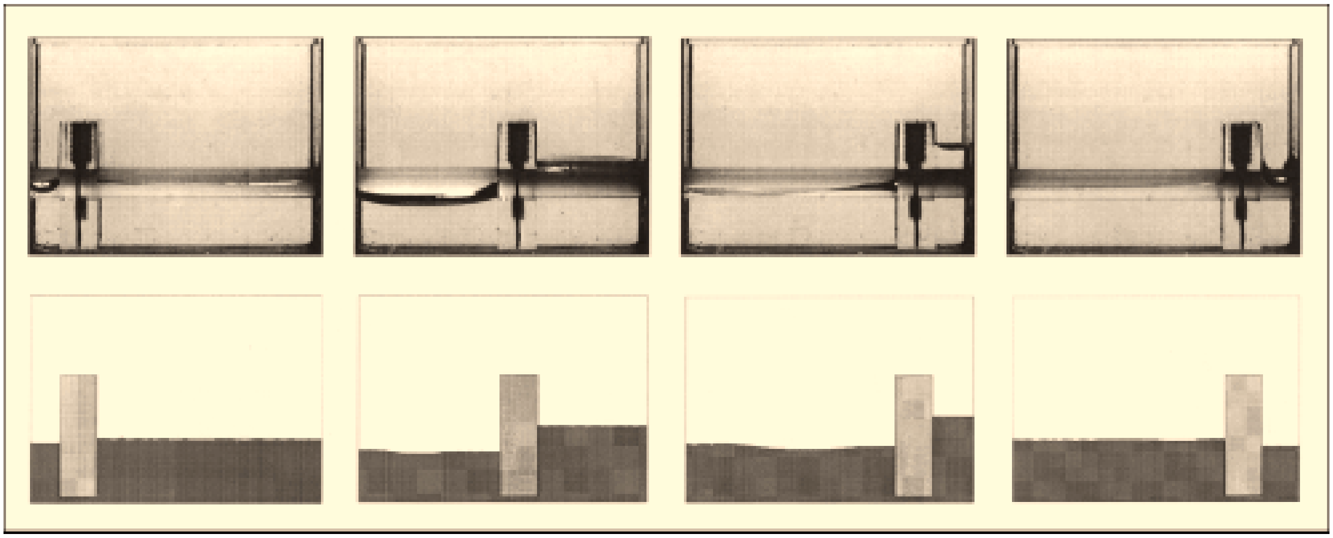

Figure 6. Free surface at different times for water at low speed.

From left to right: $t^* = 0.00$; $t^* = 0.19$; $t^* = 0.44$; $t^* = 0.50$. Experiments are shown on the top row.

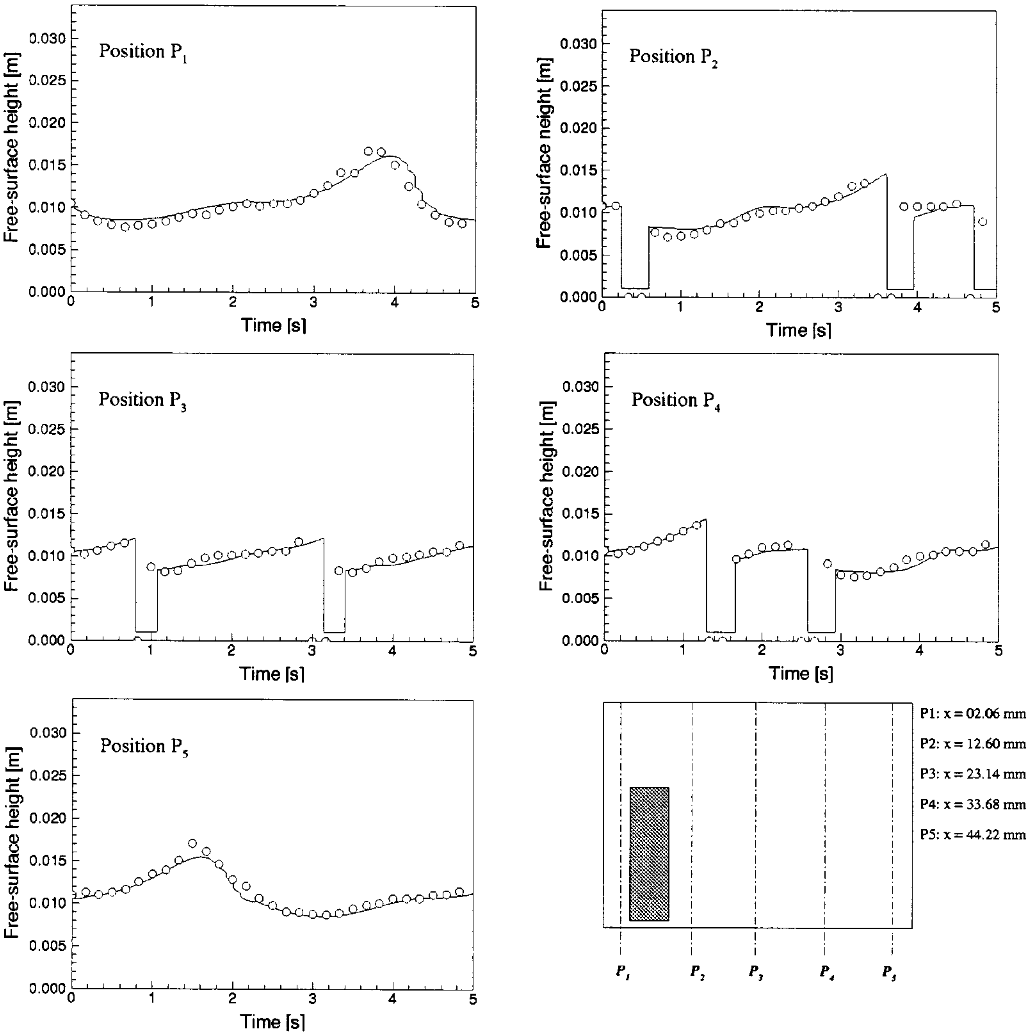

Figure 7. Free-surface height comparison: water at low speed.

○: experiments; ———: simulations.

ments, which introduces a variation of the free-surface shape in the z-direction and may significantly affect its height.

Similar to what occurs in the experiments, a large air bubble is enclosed in the oil phase after the first half-cycle, when the free-surface merging occurs. However, in the simulations the bubble progressively disappears as the ram continues over the rest of the cycle (not shown here), whereas the bubble remains visible in the experiments. This spurious effect can be easily explained. The discretization cannot maintain structures (i.e., sharp gradients of ϕ) that have a size comparable to the grid cells, even with the use of the interface-sharpening algorithm. Any small structure will be progressively smeared out in time due to numerical diffusion. Overall mass conservation is nevertheless guaranteed by the interface-sharpening algorithm (CFDS, 1995). This means that effects such as air entrapment or bubble inclusion can only be captured with a VoF method at sizes much larger than the mesh. In other words, and this is obvious, Euler volume-tracking methods should be used to capture the dynamics of phases that are segregated on scales much larger than the mesh size.

A more quantitative comparison between the simulations and the experimental results is shown on Figure 5 over one cycle. Note that the height measurements are reconstructed from the video images taken during the experiments. Due to the curvature of the free surface in the z-direction close to the front and back walls of the cavity, there is an inherent ambiguity on the exact height of the free surface, which is not present in the simulations, since these were performed on a two-dimensional domain. Note also that in the case of multiple values (folding of the free surface), the image analysis algorithm did extract only the lowest value of the free-surface height. As can be seen in the figure, there is good agreement between the simulations and the experimental results, especially for the points P_2, P_3, and P_4. Note also that due to the coating occurring on the side walls, the error at points P_1 and P_5 will be larger due to the large slope of the free surface in these regions.

Water at 16 rpm

In the case of water at low agitation speed, the hydrostatic pressure difference between both sides of the ram drives a backflow in the small gap under the ram that is large enough to prevent the water to flow over the ram, as seen in Figure 6. Due to the low viscosity of the water as compared to the silicon oil, the coating on the side walls drains very fast, and no film is visible on either side. The comparison of the time evolution of the free-surface height at several locations shown

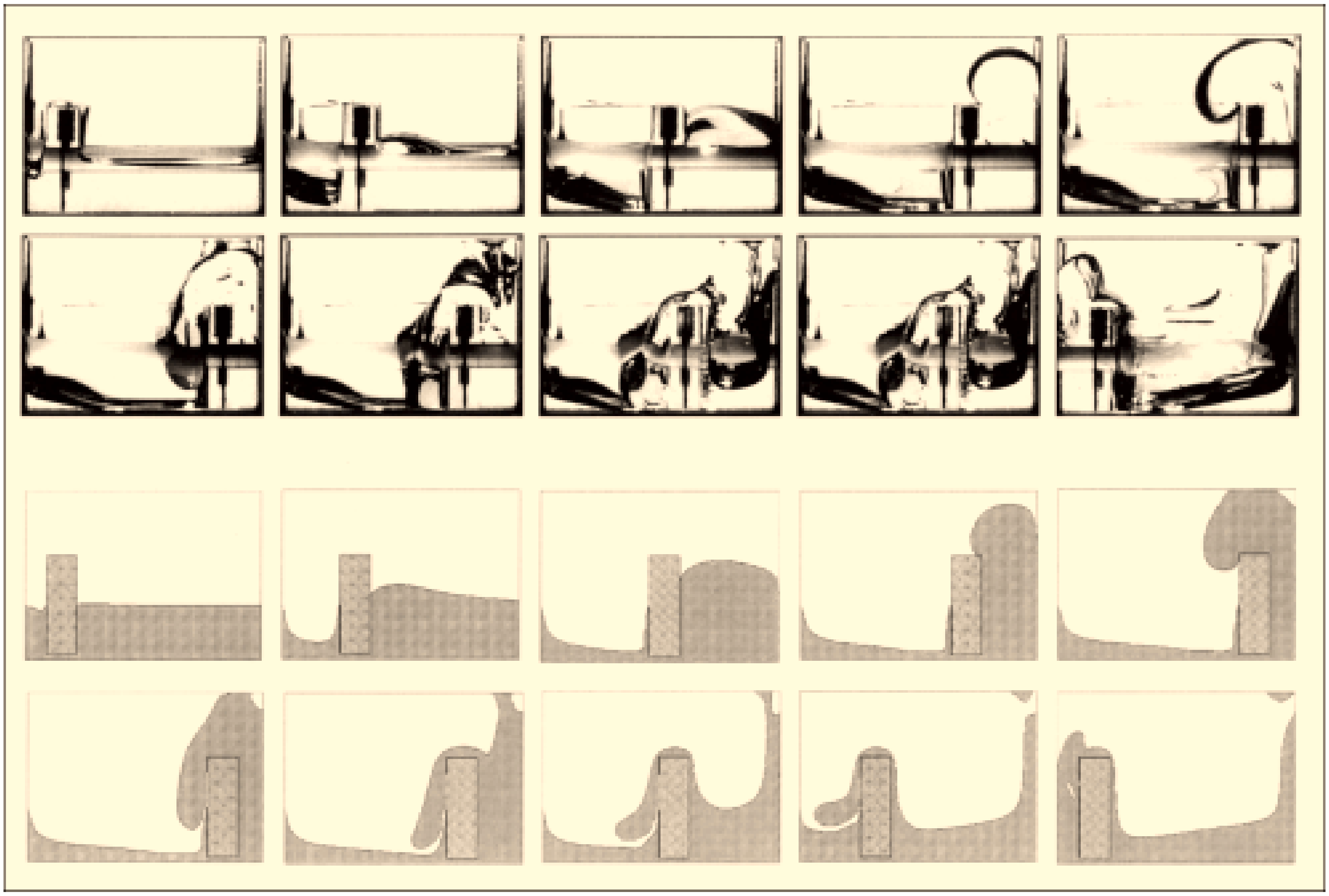

Figure 8. Free surface at different times for silicon oil at high speed.

From left to right: $t^* = 0.00$; $t^* = 0.10$; $t^* = 0.18$; $t^* = 0.38$; $t^* = 0.44$; $t^* = 0.50$; $t^* = 0.56$; $t^* = 0.62$; $t^* = 0.76$; $t^* = 0.94$. Experiments are shown on the top row.

in Figure 7 gives an excellent agreement between the simulation and the experimental results.

Oil at 62 rpm

As seen from the sequence shown in Figure 8, mechanisms as complex as coating, filament formation, breakup, and bubble coalescence are all present and captured in this challenging case. As the ram approaches its extreme right position, the squeezed oil volume reaches the top wall of the cavity, and adheres to it. Although the bulk of the oil falls down under gravity, a filament is formed, which eventually breaks, leaving a drop of oil on the ceiling. Once again, nonuniformity in the *z*-direction makes the experimental snapshots less clear.

The odd shape of the volume of oil that has passed over the ram and reconnects with the liquid level on the other side may be qualitatively explained by the fact that the simulations have been carried out in a two-dimensional, closed domain. Since there is no mechanism for the air to escape in the third dimension, the only possibility for the spilled-over oil to reconnect with the layer below it is to push the in-between layer of air away faster to the left. Because the ram itself is already pushing both the oil and the water in that direction, it becomes even more difficult to expel that layer of air, and the oil layer seems to be "floating" over it. Figure 9 shows the evolution of the free-surface height at various fixed x positions. In this case also, the agreement between the simulation and the experiment are good, bearing in mind that the curvature of the free surface in the third dimension (z-direction) makes it difficult to accurately measure the free-surface height. Also, as already mentioned, in the case of the multiple values of the free surface height, only the lowest experimental point was measured. (This explains why

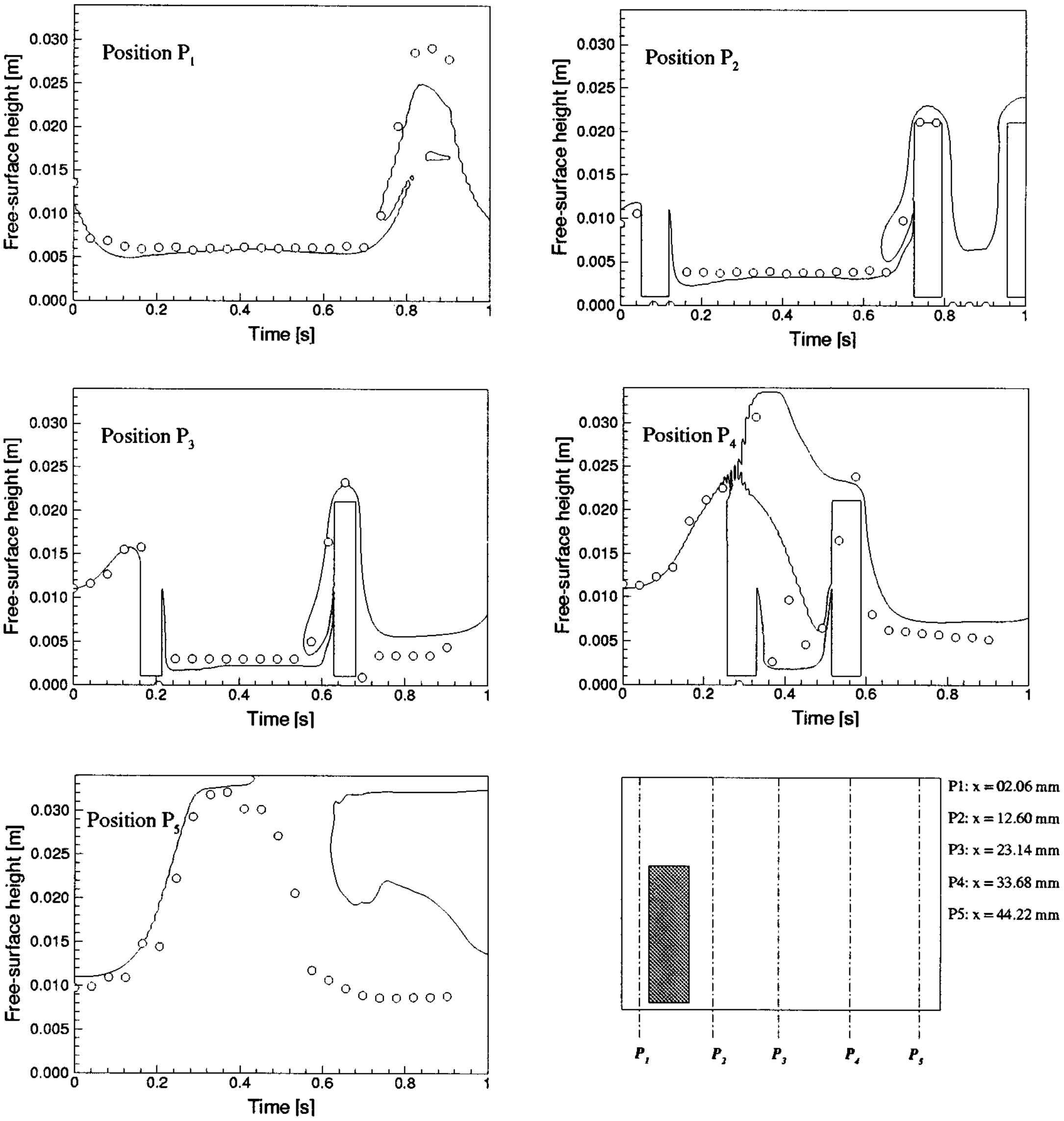

Figure 9. Free-surface height comparison: silicon oil at high speed.

○: experiments; ——: simulations.

the bubble sticking on the ceiling of the cavity is not found back in the experimental data at point P_5.)

Water at 62 rpm

Finally, the wave generation and reflection phenomena occurring in the case of water at high agitation speed are shown in Figure 10. In this case, the interface shape changes very fast, with waves traveling along the free surface across the cavity. The highly dynamic regions of surface spillover and merger show a clear three-dimensionality that is probably enhanced by the presence of the shaft in the cavity. Nevertheless, the overall agreement between the simulations and the experimental results is strikingly good, showing that the main characteristics of the free-surface topology are captured (e.g., height of the water front on the side walls, shape and extent of the spill-over flow, wave shedding).

This is confirmed by the comparisons between the evolution of the computed and the experimental free-surface height at several positions, shown in Figure 11. Here it also should be noted that in the case of multiple values in the experimental free-surface height, only the lowest value has been extracted.

Conclusions

The suitability of the VoF method has been assessed for an application to the simulation of a free-surface flow induced by an internal moving body. An experimental “mouth-analog” setup consisting of a cavity partially filled with a liquid and agitated by a ram moving periodically has been modeled and simulated. In order to test the method over a range of situations relevant to in-mouth consumption of liquid foods, two different liquid viscosities and two different agitation frequencies have been used. As the comparisons have shown, most features of the complex free-surface deformation could be captured by the simulations, including the bulging over the ram, the coating on the side and top walls of the cavity, the filament formation and breakup, and the free-surface reconnection. However, it has also been shown that maintaining structures of a size comparable to the mesh cells is not possible within the context of this Euler volume-tracking method, and the topological changes of the interface between two nonmiscible phases can only be captured for phases that are segregated on a scale significantly larger than the mesh size. Also in this essentially transient problem, a surface-sharpening algorithm is required. With the mesh sizes used, numerical diffusion would very rapidly spread the interface over a large portion of the domain. As expected from

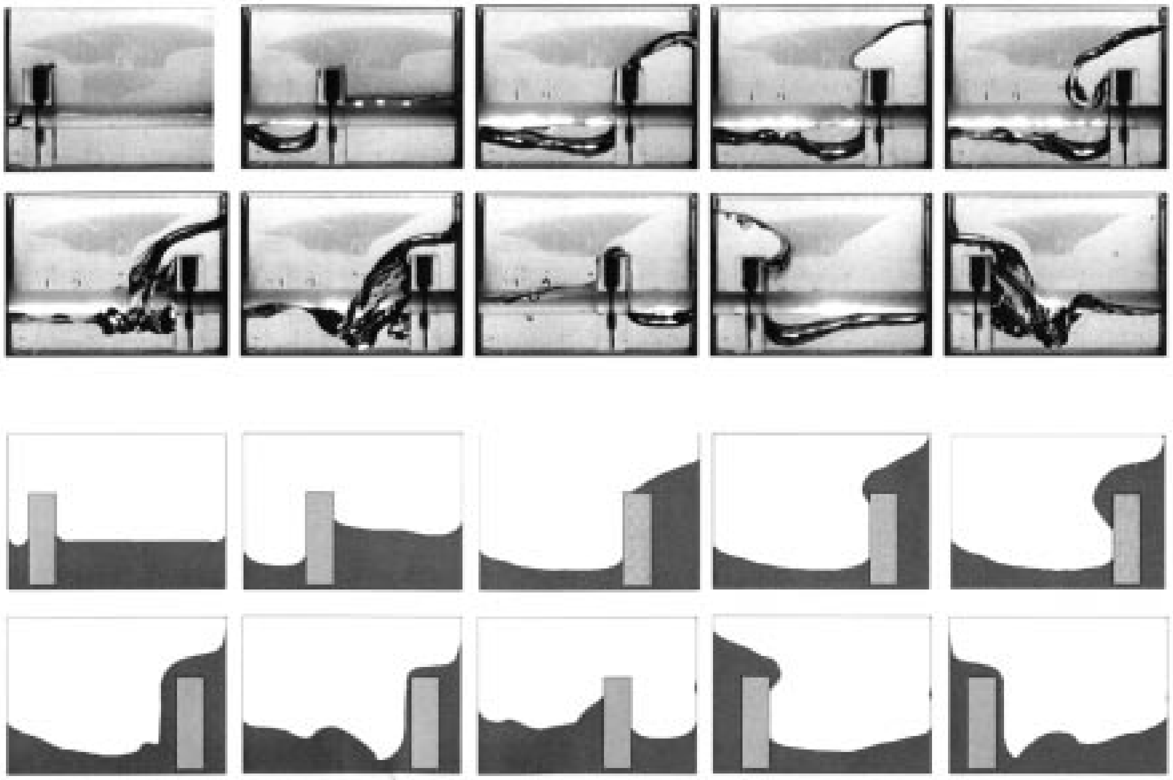

Figure 10. Free surface at different times for water at high speed.

From left to right: $t^* = 0.00$; $t^* = 0.15$; $t^* = 0.35$; $t^* = 0.42$; $t^* = 0.44$; $t = 0.46$; $t^* = 0.50$; $t^* = 0.62$; $t^* = 0.94$; $t^* = 1.00$. Experiments are shown on the top row.

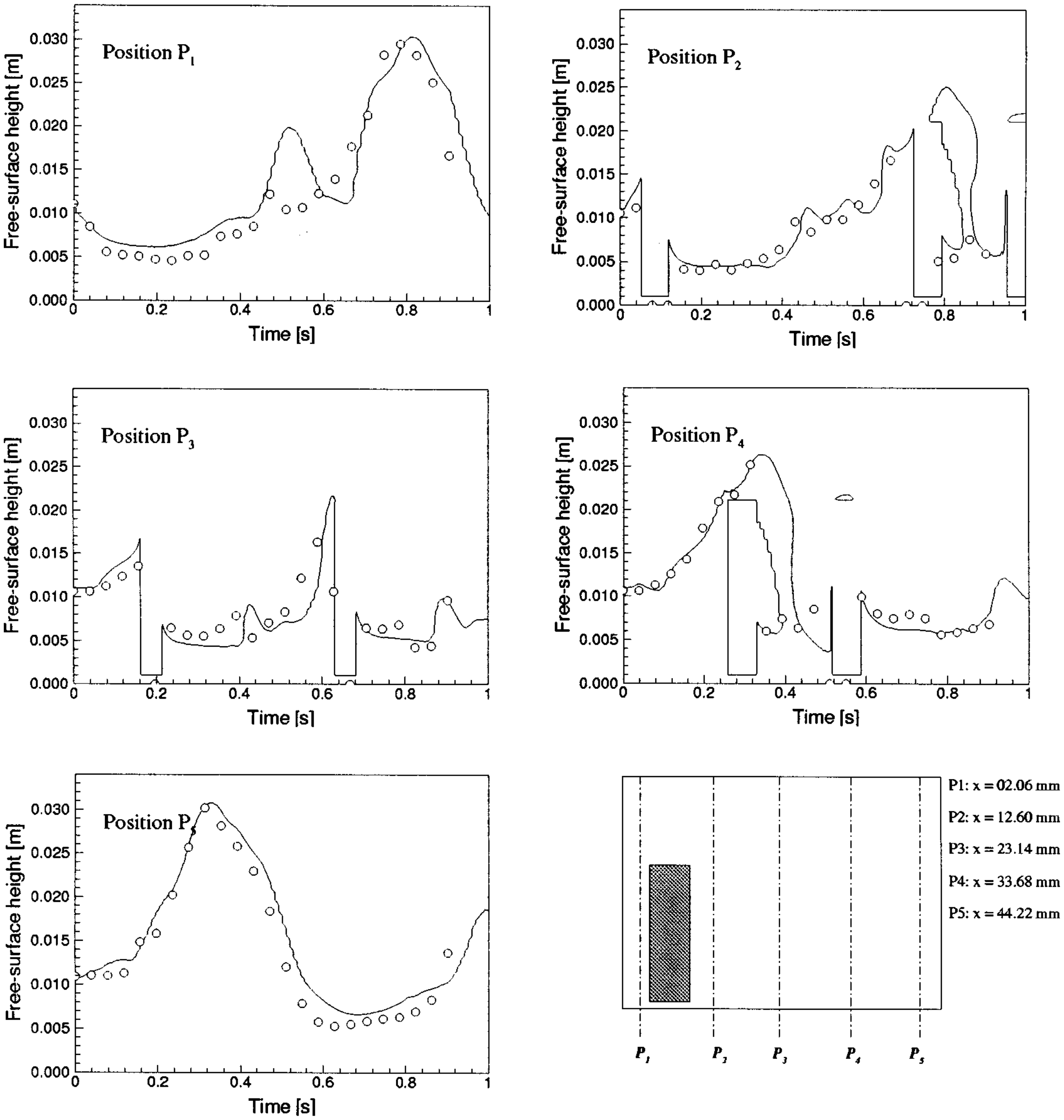

Figure 11. Free-surface height comparison: water at high speed.

○: experiments; ——: simulations.

the length scales considered in the present experimental setup, inclusion of surface tension and wall contact effects are also critical. Some spurious effects observed in the simulations, such as the persistence of an air layer under the silicon oil after bulging over the ram could be explained by the fact that the simulations were performed in a two-dimensional domain.

In conclusion, even with the large mesh and time-step sizes used in the computations, the representation of the main relevant bulk kinematics of the complex transient free-surface flow studied is possible with the VoF method, as shown earlier. This opens the way for future work related to the study of in-mouth processes, such as the relation between the sensory perception of food consumption and the time and space distribution of stresses on the boundaries of the oral cavity, the influence of coating and drainage on the mouthfeel, and the effect of mixing on the release of flavors to the nasal cavity.

Literature Cited

Brackbill, J. U., D. B. Kothe, and C. Zemach, “A Continuum Method for Modelling Surface Tension,” *J. Comput. Phys.*, **100**, 335 (1992).

Burt, D. J., J. Ferguson, and H. Pordal, “Numerical Modelling of Surface Tension Effects,” *Proc. of the ASME Fluids Engineering Division Summer Meeting*, Vol. 3, San Diego, CA (1996).

CFDS, *CFX 4.2 Flow Solver User Guide*, Computational Fluid Dynamics Services, AEA Technology, Harwell, Oxon, UK (1995).

Donea, J., S. Giuliani, and J. P. Halleux, “An Arbitrary Lagrangian-Eulerian Finite Element Method for Trasient Dynamic Fluid-Structure Interactions,” *Comput. Methods Appl. Mech. Eng.*, **33**, 689 (1982).

Hirt, C. W., A. A. Amsden, and J. L. Cook, ‘Arbitrary Lagrangian-Eulerian Computing Method for all Flow Speeds,” *J. Comput. Phys.*, **14**, 227 (1974).

Hirt, C. W., and B. D. Nichols, "Volume of Fluid (VoF) Method for the Dynamics of Free Boundaries," *J. Comput. Phys.*, **39**, 201 (1981).

Lafaurie, B., S. Zaleski, and G. Zanetti, "Modelling Merging and Fragmentation in Multiphase Flows with SURFER," *J. Comput. Phsy.*, **133**, 134 (1994).

Patankar, S. V., *Numerical Heat Transfer and Fluid Flow*, Hemisphere, New York (1980).

Rhie, C. M., and W. L. Chow, "Numerical Study of the Turbulent Flow Past an Airfoil with Trailing Edge Separation," *AIAA J.*, **21**, 1527 (1983).

Tezduyar, T. E., M. Behr, J. Liou, and S. Mittal, "A New Strategy for Finite-Element Computations Involving Moving Boundaries and Interfaces—The Deforming-spatial-domain/space-time procedure," *Comput. Methods Appl. Mech. Eng.*, **94**, 353 (1992).

Ubbink, O., and R. I. Issa, "A Method for Capturing Sharp Fluid Interfaces on Aribtrary Meshes," *J. Comput. Phys.*, **153**, 26 (1999).

Manuscript received Feb. 12, 2001, and revision received Aug. 27, 2001.